SCIENCE CHINA
Physics, Mechanics & Astronomy

•Article•

April 2023 Vol. 66 No. 4: 246112
https://doi.org/10.1007/s11433-022-2061-2

Entropy-driven atomic activation in supercooled liquids and its link to the fragile-to-strong transition

Wei Chu[1], Zheng Wang[1*], Nannan Ren[1,2], Bangshao Dong[3], Jinhua Yu[1], Pengfei Guan[2], Yanhui Liu[4], Yuanzheng Yue[5], and Lina Hu[1*]

[1] *Key Laboratory for Liquid-Solid Structural Evolution and Processing of Materials (Ministry of Education), Shandong University, Jinan 250061, China;*
[2] *Beijing Computational Science Research Center, Beijing 100193, China;*
[3] *Central Iron & Steel Research Institute, Advanced Technology & Materials Co. Ltd, Beijing 100081, China;*
[4] *Institute of Physics, Chinese Academy of Sciences, Beijing 100190, China;*
[5] *Department of Chemistry and Bioscience, Aalborg University, Aalborg 9220, Denmark*

Received November 22, 2022; accepted January 3, 2023; published online March 2, 2023

As a common but critical dynamic crossover in glass-forming liquids (GFLs), the discovery of fragile-to-strong (F-S) transition promises a novel route for understanding supercooled liquid and glass transition. The present work, for the first time, successfully realizes the quantitative prediction of the F-S transition in nine metallic glass-forming liquids, by a counter-intuitive approach that focuses on local atomic activation events, rather than relaxation, upon cooling. The dynamic crossover originates from a disorder-to-order transition by self-regulating behavior of atomic position within a cage controlled by finite atomic activation events, due to the appearance of local cooperative motion of nearest neighborhood atoms. Moreover, the dominant role of entropy in this anomaly has been discovered, and the correspondence between the crossover of configuration entropy involved in activation events and the occurrence of F-S transition has been found. Our work implies that the feature of atomic energy fluctuations reflected by atomic activation events has a close linkage to complex dynamic behaviors of disordered systems.

metallic glass, fragile-to-strong transition, supercooled liquid, entropy control

PACS number(s): 02.70.Ns, 61.20.Ja, 64.70.Ja, 81.05.Kf

Citation: W. Chu, Z. Wang, N. Ren, B. Dong, J. Yu, P. Guan, Y. Liu, Y. Yue, and L. Hu, Entropy-driven atomic activation in supercooled liquids and its link to the fragile-to-strong transition, Sci. China-Phys. Mech. Astron. **66**, 246112 (2023), https://doi.org/10.1007/s11433-022-2061-2

1 Introduction

Despite considerable progress in understanding the complex transition processes from liquids to glasses [1,2], many key questions remain unanswered [3]. The dynamics of supercooled liquids are believed to be a key to answering those questions. Among several dynamic crossovers observed in liquids [4-7], the so-called fragile-to-strong (F-S) transition in deep supercooled liquids attracts much attention [8-11]. Angell [12] introduced the concept of liquid fragility, which is defined as the changing rate of liquid viscosity η or relaxation time τ with temperature at the glass transition temperature T_g. The systems exhibiting the Arrhenian dependence of $\log\eta$ (or $\log\tau$) vs. T_g/T are defined as "strong" liquids, while those exhibiting non-Arrhenian dependence are defined as "fragile" liquids. However, some liquids exhibit the F-S transition during cooling. Since this transition was discovered in water [13], the F-S transition has been observed in many liquid systems such as silica [14], BeF_2

*Corresponding authors (Lina Hu, email: hulina0614@sdu.edu.cn; Zheng Wang, email: zheng.wang@sdu.edu.cn)

[15], and metals [11,16]. The F-S transition in glass-forming liquids (GFLs) is a striking dynamic feature [11,16,17]. The extrapolations of the high-temperature (HT) and low-temperature (LT) viscosity curves result in an intersection temperature $T_{\mathrm{F\text{-}S}}^{\eta}$ (i.e., the F-S transition temperature) in the deep supercooled region [11]. The intersection indicates that the liquid undergoes a nonlinear dynamic evolution upon cooling. Revealing the mechanism of the F-S transition is crucial for understanding the glass formation. However, the strong crystallization tendency in the supercooled region is the main barrier to observing the details of the F-S transition.

Theoretical explanations have been proposed to rationalize this interesting F-S transition in GFLs from different perspectives, such as local structure competition [8,11], polyamorphic transformation [9], and separation of α/β relaxation [18], and show the success of reproducing the anomaly qualitatively [8,10]. It is worth noting that the central idea of previous attempts only focuses on the relaxation of the system upon cooling. Among them, the most popular view is to attribute the F-S transition to a transition between two states of liquids, like a crossover from high-density/non locally-favored structure liquid to low-density/locally-favored structure liquid [10,19]. For some network glasses or water, the two-state scenario looks reasonable, but whether it is the exclusive origin of the F-S transition remains controversial. Many glasses, especially metallic glasses (MGs), do not show such a distinct state divergence in liquids from experiments [20-22]. The non-directional metallic bonding of MGs makes it an ideal system to study the universal intrinsic origin of the F-S transition. However, the results of relevant studies in MGs are far from satisfactory, and the F-S transition cannot be observed from the simulated dynamic results [23,24], i.e., from the temperature dependence of relaxation time or viscosity of systems.

In this work, we study the F-S transition from a new perspective, i.e., by focusing on finite atomic activation events on the fluctuations of atomic potential energy at different temperatures. This allows a quantitative prediction of the F-S transition and a derivation of its characteristic values in nine metallic glass-forming liquids (MGFLs). This dynamic crossover was found to originate from the transition from disordered to ordered diffusion of the activated atoms, i.e., an entropy-driven process. The present work indicates that the fluctuation feature of atomic potential energy, which is dependent on temperature, has a close linkage to the dynamics of systems.

2 Model and simulation methods

2.1 Simulation details

Molecular dynamic simulations were carried out for nine MGFLs by using the Large-scale Atomic/Molecular Massively Parallel Simulator (Lammps) [25] based on the many-body embedded atom method (EAM) potentials. In short, the interatomic potential is obtained by fitting the potential energy surface of the system. The potential energy of an embedded atom i is given by $E_i = F_\alpha\left(\sum_{j\neq i}\rho_\beta(r_{ij})\right)+\left(\sum_{j\neq i}\phi_{\alpha\beta}(r_{ij})\right)/2$, where F is the embedding energy which is a function of the atomic electron density ρ, ϕ is a pair potential interaction, and α and β are respectively the element types of atoms i and j. We have performed molecular dynamics simulations in nine different MGFLs, mainly including seven CuZr liquids ($Cu_{48}Zr_{52}$, $Cu_{50}Zr_{50}$, $Cu_{52}Zr_{48}$, $Cu_{54}Zr_{46}$, $Cu_{56}Zr_{44}$, $Cu_{58}Zr_{42}$, and $Cu_{60}Zr_{40}$), $Cu_{49}Zr_{49}Al_2$ liquid, and $Fe_{80}P_{20}$ liquid. Among them, the interatomic interactions of the CuZr system and CuZrAl system were described by Cheng et al. [26,27], and the interatomic interactions of the FeP system were described by Ackland et al. [28]. For reasons of computational efficiency, all systems contain 8000 atoms, except $Cu_{50}Zr_{50}$ which contains 16000 atoms as a typical example. The periodic boundary conditions were applied in three directions for all systems. Under the isobaric-isothermal ensemble (NPT), all samples were first equilibrated above the liquidus temperature for a long enough time (about 2 ns). Then the sample was quenched to 300 K at the cooling rate of 1 K/ps and independent configurations at different temperatures were selected for further relaxation. After adequate relaxation at each temperature, the ensemble was converted to the NVT ensemble, and 2000 configurations were collected for FAAM calculation in 4 ps. The purpose of selecting the configurations in this way is to ensure that the output atomic potential curves are detailed enough to better capture the short-time atomic activation events. Although this approach is not considered an equilibrium calculation, our calculations show that the results obtained in this way are equivalent to those under equilibrium calculations (see Supplementary Materials for details). In contrast, the total time spanned by the configurations used for the dynamic analysis is as large as possible compared to the relaxation time of the system. In this case, calculations based on equilibrium states are guaranteed. In all simulations, the timestep is 2 fs and the temperature are controlled by the Nose-Hoover thermostat [29]. In the calculation of the configuration entropy, the atomic structure of the alloy was analyzed by the Voronoi tessellation method [30] using the Voro++ package. The glass transition temperature T_g at this cooling rate was defined by the crossover of the curve of the E–$3k_BT$ versus T (see Figure S1 for details), where E stands for the total energy and k_B for the Boltzmann constant.

2.2 Finite atomic-activation method (FAAM)

According to the classic Energy Landscape Theory (ELT), there are numerous accessible energy poles (energy barrier)

and basins (inherent states) for a given material system [3], as shown in Figure 1(a). The potential energy of the system gradually decreases upon cooling, as illustrated in Figure 1(b) (gray circles). Relaxation is the dominant dynamic process of the liquid, which is a hopping process from a high- to a low-energy basin, i.e., an energy reduction of the system [3,31,32]. In contrast, activation is a reverse process of relaxation, which is a similar "tramp over hill and dale" of potential energy, but eventually lifts the energy [33]. This process of a system being activated to a higher energy state is also known as rejuvenation [34,35]. For a bulk system, activation is difficult to be naturally achieved and can be realized only by external treatments such as pressurization or cryogenic thermal cycling (CTC) treatment [33,36]. However, if it comes to the atomic level, the atomic activation (energy elevation) could generally occur in liquids, required by a kinetic equilibrium. Figure 1(c) and (d) show the potential energy change of a randomly selected atom (as an example) in $Cu_{50}Zr_{50}$ liquid at 1800 and 900 K, respectively. Much like that in the Potential Energy Landscape (PEL) in shape, there are also many basins, which are due to the energy fluctuations. It is seen that the atomic potential energy is changing with time (t) at a constant temperature. During the change of energy with time (steps), the local relaxation event (marked by black arrows) and local activation event (marked by green arrows) will always occur over time. The local

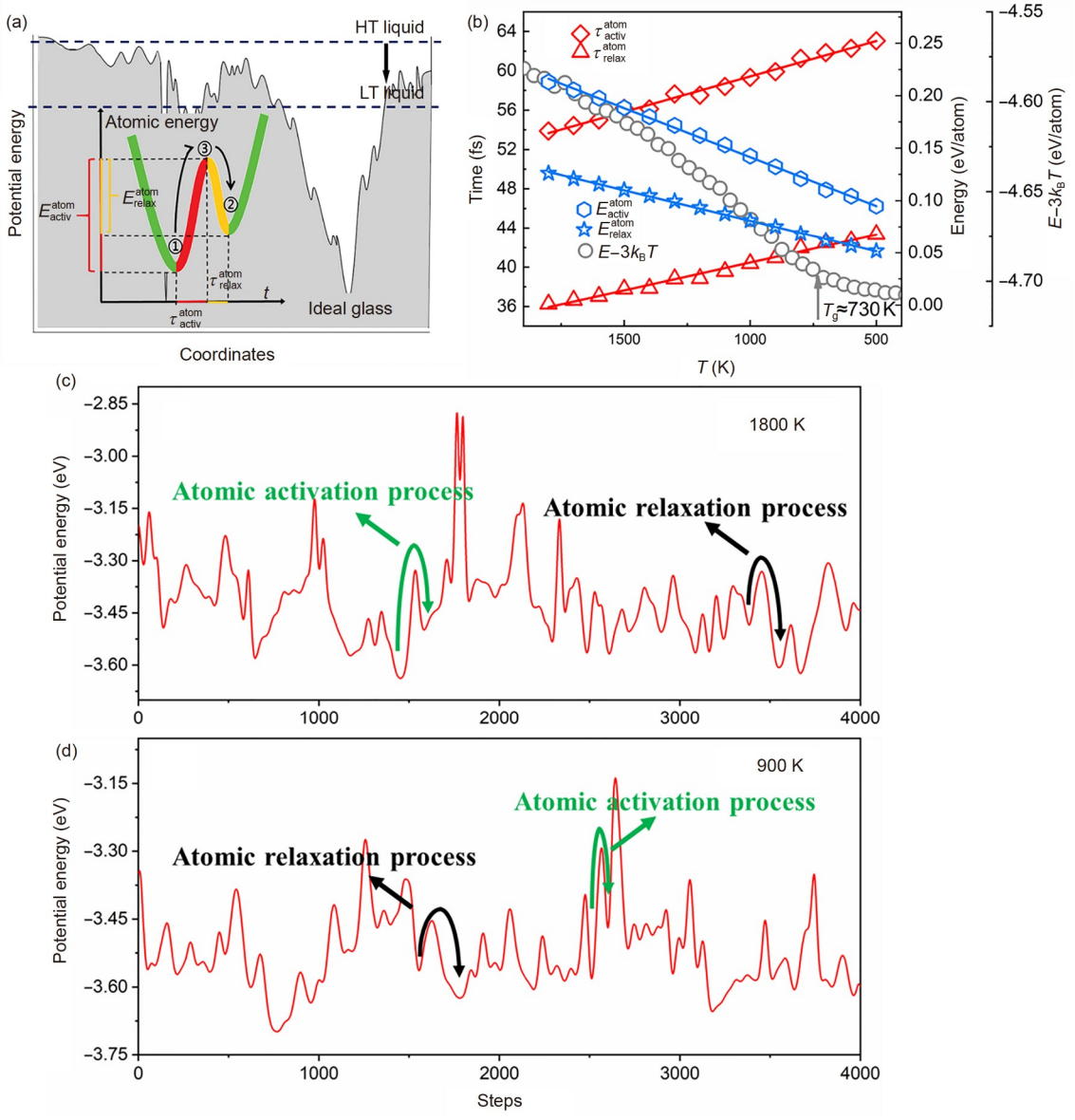

Figure 1 (Color online) (a) Schematic illustration of the potential energy landscape (PEL) and the atomic activation process (inset). (b) Temperature dependence of atomic activation time τ_{activ}^{atom}, relaxation time τ_{relax}^{atom}, activation energy E_{activ}^{atom}, relaxation energy E_{relax}^{atom}, and the $E-3k_BT$ for $Cu_{50}Zr_{50}$ liquid upon cooling. The atomic potential energy change of a randomly selected atom in 4000 steps at (c) 1800 K, and (d) 900 K for $Cu_{50}Zr_{50}$ liquid. The black and green arrows represent the local atomic relaxation and activation process, respectively, which are shown as examples here.

relaxation event here refers to the process of moving from a high-energy basin into another lower-energy basin, while the local activation event is the opposite. Notice that Figure 1(c) and (d) only point to one atom as an example. The same situation exists for all atoms. In the present work, the local atomic activation events are more attractive to us than the local relaxation ones. Therefore, we collected and analyzed the characteristics of these local activation events at different temperatures. The statistical analysis of these atomic activation events is named as Finite Atomic Activation Method (FAAM). This method relies only on the interactions among atoms described by the potential functions, and no more assumptions are introduced.

A more detailed illustration of one atomic activation event was shown in the left-lower inset of Figure 1(a), where the abscissa and the ordinate represent time (t) and the atomic potential energy, respectively. It can be viewed as two consecutive basins intercepted from the atomic potential energy curve. Points 1 and 2 represent two different neighboring basins on the potential energy change curve of one atom, where the energy at point 2 is higher than that at point 1, whereas point 3 represents the transition state between them. The whole activation event can be divided into two parts: the activation stage from point 1 to 3 (step 1), and then the relaxation stage from point 3 to 2 (step 2). We defined the time for the atomic potential energy to complete the activation stage (step 1) and the relaxation stage (step 2) as $\tau_{\text{activ}}^{\text{atom}}$ and $\tau_{\text{relax}}^{\text{atom}}$, respectively. The energy changes after the completion of stages 1 and 2 were defined as $E_{\text{activ}}^{\text{atom}}$ and $E_{\text{relax}}^{\text{atom}}$, respectively. At each temperature, based on the atomic potential energy change curves obtained by Lammps software (see Figure 1(c) and (d)), we collected all the intervals of atomic activation events for all atoms and calculated the four parameters based on our two-step classification. These four parameters could describe the characteristics of one atomic activation event, and their final values at each temperature are the result of averaging a large amount of statistical data. Detailed statistics and calculation procedures have been presented in Supplementary Materials. Figure 1(b) shows the variation of these four parameters in $Cu_{50}Zr_{50}$ liquid during cooling. The energy ($E_{\text{activ}}^{\text{atom}}$ and $E_{\text{relax}}^{\text{atom}}$) decreases monotonically with the lowering of the temperature, and the gap between these two energies narrows. Meanwhile, the time ($\tau_{\text{activ}}^{\text{atom}}$ and $\tau_{\text{relax}}^{\text{atom}}$) increases monotonically with decreasing temperature. The local activation event is a process of energy elevation, and $E_{\text{activ}}^{\text{atom}}$ must be higher than $E_{\text{relax}}^{\text{atom}}$. Since the atomic potential energy change is continuous, it is reasonable to spend more time completing the activation stage than the relaxation stage for one atom ($\tau_{\text{activ}}^{\text{atom}} > \tau_{\text{relax}}^{\text{atom}}$).

The starting point of FAAM is essentially the same as the hopping phenomenon in supercooled water [37], but our study of atomic activation stops at the ballistic regime, the essence of which is an adjustment of atomic positions within the cage, as demonstrated subsequently. In addition, FAAM can capture steps 1 and 2 of one atom over the whole temperature range, which has a distinct advantage over the classic "two-level system" model suitable only for the low-temperature range [38]. A computational approach called the activation-relaxation technique (ART) [39] has been widely used to study the relaxation of continuous disordered systems and shows its successes [40]. There is also a similar method known as the nudge elastic band (NEB) calculation [41-43]. However, both methods (ART and NEB) target the whole system and aim to find the minimum energy path between different states of the system on the potential energy surface. In contrast, FAAM in this work targets the fluctuation feature of atomic potential energy to find its correlation with system dynamics.

2.3 Analysis of the F-S transition

(1) The equilibrium viscosity of a glass-forming liquid can be described by the Mauro-Yue-Ellison-Gupta-Allan (MYEGA) [44] equation:

$$\lg\eta = \lg\eta_\infty + \frac{B}{T}\exp\left(\frac{C}{T}\right), \tag{1}$$

where η_∞ is the high-temperature viscosity limit [44,45], T is the absolute temperature, and B and C are fitting parameters. Combining eq. (1) with the definition of fragility $m = \left.\frac{\mathrm{d}\log\eta}{\mathrm{d}(T_\mathrm{g}/T)}\right|_{T=T_\mathrm{g}}$, m_{LT} can be obtained by fitting the low-temperature part of viscosity as:

$$m_{\text{LT}} = \frac{B}{T_\mathrm{g}}\left(1+\frac{C}{T_\mathrm{g}}\right)\exp\left(\frac{C}{T_\mathrm{g}}\right). \tag{2}$$

The fragility from the high-temperature part of viscosity-m_{HT} also can be obtained by the same method. A parameter f was proposed previously to measure the degree of F-S transition by [16]

$$f = \frac{m_{\text{LT}}}{m_{\text{HT}}}. \tag{3}$$

(2) An extended MYEGA model has been proposed to describe the viscosity changes in MGFLs exhibiting the F-S transition [46]:

$$\log_{10}\eta = \log_{10}\eta_\infty + \frac{1}{T\left[W_1\exp\left(-\frac{C_1}{T}\right)+W_2\exp\left(-\frac{C_2}{T}\right)\right]}, \tag{4}$$

where C_1 and C_2 correspond to the constraint onsets reflecting dynamic mechanisms at HT and LT, respectively, and the fitted W_1 and W_2 parameters represent weight coefficients. It has been found the fitting curves well fit the viscosity of alloy liquids in the whole temperature range

[11,16]. According to eq. (4), the temperature $T_{\text{F-S}}^{\eta}$ at which the F-S transition occurs, is defined as follows [11]:

$$W_1\exp\left(-\frac{C_1}{T_{\text{F-S}}^{\eta}}\right)=W_2\exp\left(-\frac{C_2}{T_{\text{F-S}}^{\eta}}\right).$$

Then

$$T_{\text{F-S}}^{\eta}=\frac{C_1-C_2}{\ln W_1-\ln W_2}. \quad (5)$$

3 Results

3.1 F-S transition in $Cu_{50}Zr_{50}$ liquid

To describe the competition between activation and relaxation steps, we defined a time-related parameter, $\gamma_{\tau}^{\text{atom}}=\frac{\tau_{\text{relax}}^{\text{atom}}}{\tau_{\text{activ}}^{\text{atom}}}$. As a representative, the temperature dependence of $\gamma_{\tau}^{\text{atom}}$ for $Cu_{50}Zr_{50}$ liquid calculated based on FAAM is shown in Figure 2(a). $\gamma_{\tau}^{\text{atom}}$ ranges from 0.672 to 0.693 above T_g, indicating that the activation stage always takes a longer time than the relaxation stage, which is the characteristic of atomic activation events. Interestingly, when $\gamma_{\tau}^{\text{atom}}$ and the measured viscosity η are plotted in the same figure, the two parameters have almost the same change trend in either the HT or the LT regions approaching T_g. We also compare $\gamma_{\tau}^{\text{atom}}$ and η at high temperatures determined by other methods [47-50], showing a good match (Figure 2(b)). Here, $\gamma_{\tau}^{\text{atom}}$ is obtained from the atomic activation event, while η represents the macroscopic flow of the system. Even though the two parameters have different units and magnitudes, an overlap is seen in Figure 2(a), implying a connection between the microscopic thermodynamics and the macroscopic dynamics. Moreover, when extrapolating by the MYEGA equation [44] (eq. (1)) for both HT and LT liquids, a big gap between the two fitting curves is present. It is seen that the value of $\gamma_{\tau}^{\text{atom}}$

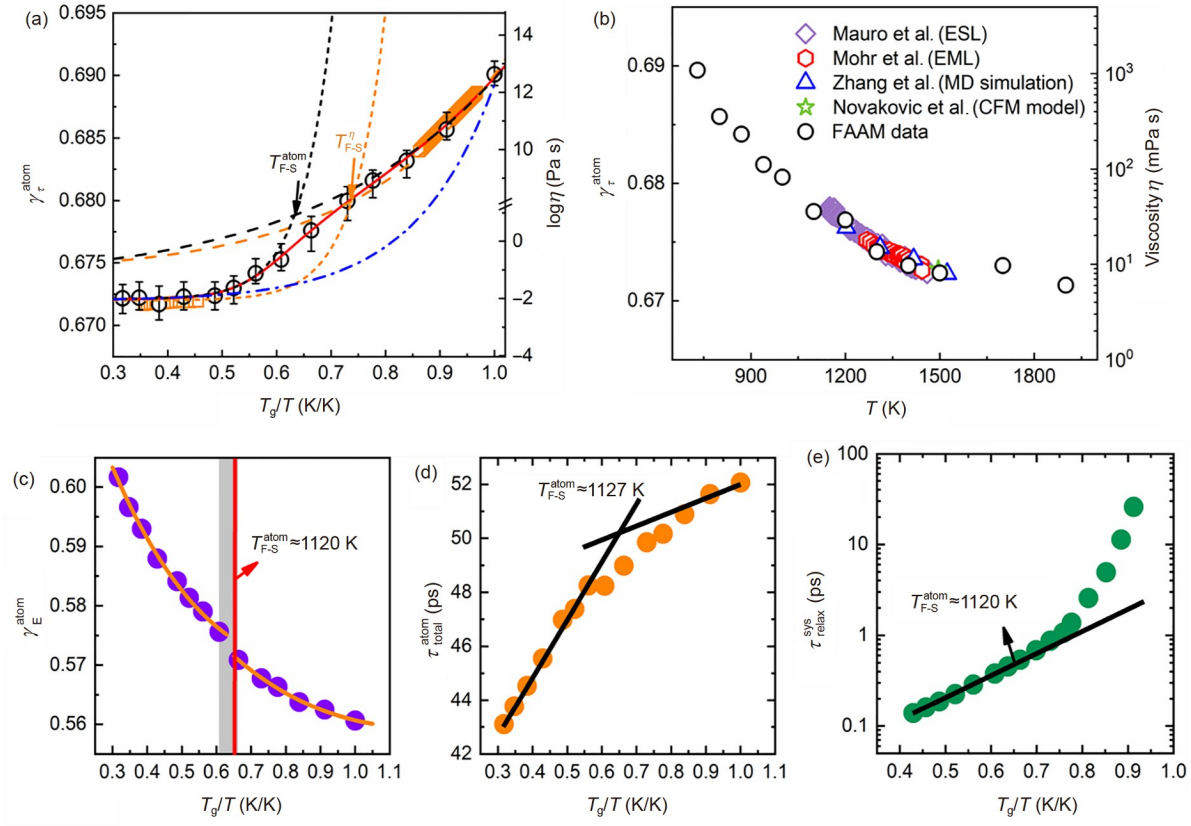

Figure 2 (Color online) (a) The comparison between $\gamma_{\tau}^{\text{atom}}$ and the experimental viscosity η for $Cu_{50}Zr_{50}$ liquid. The hollow black spheres and orange squares represent the data obtained from FAAM and viscosity measurements, respectively. The black dash and short-dash curves represent the fragile and strong dynamics of FAAM data, respectively. The orange dash and short-dash curves represent the fragile and strong dynamics of experimental viscosity, respectively. Their intersections are the characteristic temperatures: $T_{\text{F-S}}^{\text{atom}}$ and $T_{\text{F-S}}^{\eta}$ (calculated according to eq. (5)). The error bars of $\gamma_{\tau}^{\text{atom}}$ are derived from the results after three independent calculations. (b) The comparison of $\gamma_{\tau}^{\text{atom}}$ with the viscosities at high temperatures of $Cu_{50}Zr_{50}$ liquid measured by microgravity electromagnetic levitator ISS-EML (red squares), the ground-based electrostatic levitation (ESL) (purple diamonds), simulation MD results (blue triangles), and the value predicted by the CFM model at 1473 K (green pentagram). (c) The $\gamma_{\text{E}}^{\text{atom}}$ as a function of the T_g scaled temperature T for $Cu_{50}Zr_{50}$ liquid. The yellow solid curves are the fittings of the MYEGA equation. Temperature dependence of (d) total atomic relaxation time $\tau_{\text{total}}^{\text{atom}}$, and (e) fictive system relaxation time $\tau_{\text{relax}}^{\text{sys}}$. The solid lines in (d) and (e) denote the linear fitting and the Arrhenius fitting, respectively.

extrapolated from the HT region to T_g (the dash-dotted blue curve) is always smaller than the real values of γ_τ^{atom} at low temperatures, and on the contrary, the value of γ_τ^{atom} by fitting the data near T_g to the HT region (dash black curve from LT part) is always larger than the real values of γ_τ^{atom} at high temperatures. Considering the monotonic increase in both τ_{activ}^{atom} and τ_{relax}^{atom} during cooling (Figure 1(b)), it suggests that, at the atomic scale, the HT liquid behaves in activation priority, and the LT liquid is in relaxation priority. In accordance with it, the γ_τ^{atom} values in the whole temperature range are well described by an extended MYEGA model [16] (the solid curve), indicating a clear change from a fragile behavior at the HT to the strong behavior at the LT, i.e., the existence of the F-S transition in the intermediate region. The crossover temperature of (1120±22) K (~1.52T_g) which is named $T_{F\text{-}S}^{atom}$ here, can be calculated according to eq. (5). $T_{F\text{-}S}^{atom}$ is higher than $T_{F\text{-}S}^{\eta}$ (1.36T_g) (calculated based on viscosity data) as shown in Figure 2(a), agreeing with a previous study [18], where the embryo of F-S transition was suggested to occur above $T_{F\text{-}S}^{\eta}$. The F-S transition extent parameter f_{FAAM} is also determined to be 4.02, which is almost the same as f_{exp}=4.0 obtained from viscosity η measurements [11]. More details about equations and parameters can be found in the Methods part. Therefore, γ_τ^{atom} is a good parameter to reproduce the F-S transition in $Cu_{50}Zr_{50}$ glass-forming liquid.

Likewise, the same feature is also reflected by the competition between relaxation energy and activation energy in atomic activation events. Figure 2(c) shows the change of γ_E^{atom} ($\gamma_E^{atom}=\frac{E_{relax}^{atom}}{E_{activ}^{atom}}$) as a function of scaled temperature T_g/T. A lower temperature leads to a smaller γ_E^{atom}, which hints that the activation stages become more difficult than the relaxation stages for atoms. There is a crossover of the γ_E^{atom} changing tendency in a critical temperature range, marked as gray area in Figure 2(c). The $\gamma_E^{atom}-T_g/T$ relation cannot be fitted by only one MYEGA equation (orange curves) in the whole temperature range and it breaks at about (1149±53) K. This break temperature range accords with the observed F-S temperature $T_{F\text{-}S}^{atom}$ in Figure 2(a).

To further understand the role of atomic activation events in the whole relaxation of systems upon cooling, the changes of several characteristic times with temperature were systematically studied. Figure 2(d) shows the temperature dependence of the total atomic relaxation time τ_{total}^{atom}, which is the sum of τ_{activ}^{atom} and τ_{relax}^{atom} in activation events. The intersection at ~1127 K, i.e., $T_{F\text{-}S}^{atom}$, can also be obtained by linearly fitting its HT and LT data. Furthermore, the system relaxation time τ_α^{sys} was calculated from the self-intermediate scattering function *SISFs* (see Figure S2). The crossover temperature lies at 1300 K (often denoted by T_A in refs. [4,51,52]), much higher than $T_{F\text{-}S}^{atom}$. Interestingly, when we introduce a fictive system relaxation time $\tau_{relax}^{sys}=\tau_\alpha^{sys}\times\left(\frac{\tau_{relax}^{atom}}{\tau_{total}^{atom}}\right)$, τ_{relax}^{sys} deviates from the Arrhenius fit at $T_{F\text{-}S}^{atom}$ (Figure 2(e)). This means that the F-S transition induced by limited atomic motions is shadowed by the dynamic behavior of the entire system, like β relaxation at the embryonic stage that cannot be separated from α relaxation in strong metallic glasses [53]. Such an assumption concerning the F-S transition was previously proposed in Zr-based metallic glass-forming liquid [18] and in a two-dimensional colloidal suspension [54], but here we offer a clearer physical demonstration.

3.2 F-S transition in more liquids

It has been found that the strength of F-S transition is different for various MGFLs, and the f_{exp} value can range from 1.4 to 8.2 [18]. In order to further prove the ability of FAAM in predicting the F-S transition, we compare the changes of γ_τ^{atom} and the experimental η with temperature in other nine metallic glass-forming liquids, as shown in Figure 3. Similar to $Cu_{50}Zr_{50}$, Cu_xZr_{100-x} (x=48, 52, 54, 56, 58, 60) lies in the composition interval where bulk metallic glasses can be formed. In addition, $Cu_{49}Zr_{49}Al_2$ also exhibits strong glass-forming ability (GFA), and however, $Fe_{80}P_{20}$ alloy has poor GFA. Due to the lack of the viscosity data of $Fe_{80}P_{20}$, the detected viscosity of $Fe_{74}Mo_4P_{10}C_{7.5}B_{2.5}Si_2$ is used here as a reference [55]. As shown in Figure 3, the change trends of γ_τ^{atom} and viscosity are in good agreement in both HT and LT temperature regions. Like the $Cu_{50}Zr_{50}$ in Figure 2(a), all systems show a clear fragile-to-strong transition. By fitting the γ_τ^{atom} with eq. (4), the $T_{F\text{-}S}^{atom}$ for every liquid is calculated, listed in Table 1. It is seen that the $T_{F\text{-}S}^{atom}$ varies between 933.8 to 1339 K, and the $T_{F\text{-}S}^{\eta}$ varies from 904.87 to 1303 K. The T_g dependence of $T_{F\text{-}S}^{atom}$ and $T_{F\text{-}S}^{\eta}$ for all liquids is plotted in Figure 3(i). Although the T_g values from the simulation and the experiment are different, $T_{F\text{-}S}^{atom}$ and $T_{F\text{-}S}^{\eta}$ are relatively consistent. Especially, the f_{FAAM} value is very close to f_{exp} for these alloys, as shown in Table 1. It further supports that γ_τ^{atom} derived from FAAM is not only a dominant parameter determining the F-S transition, but also could realize its quantitative prediction, e.g., the viscosity change in deep supercooled liquids and the strength parameter f_{exp}. The success of FAAM supported by Figures 2 and 3 hints at the key role of the atomic activation events involved in the fluctuation of atomic potential energy in predicting the dynamics of supercooled liquids.

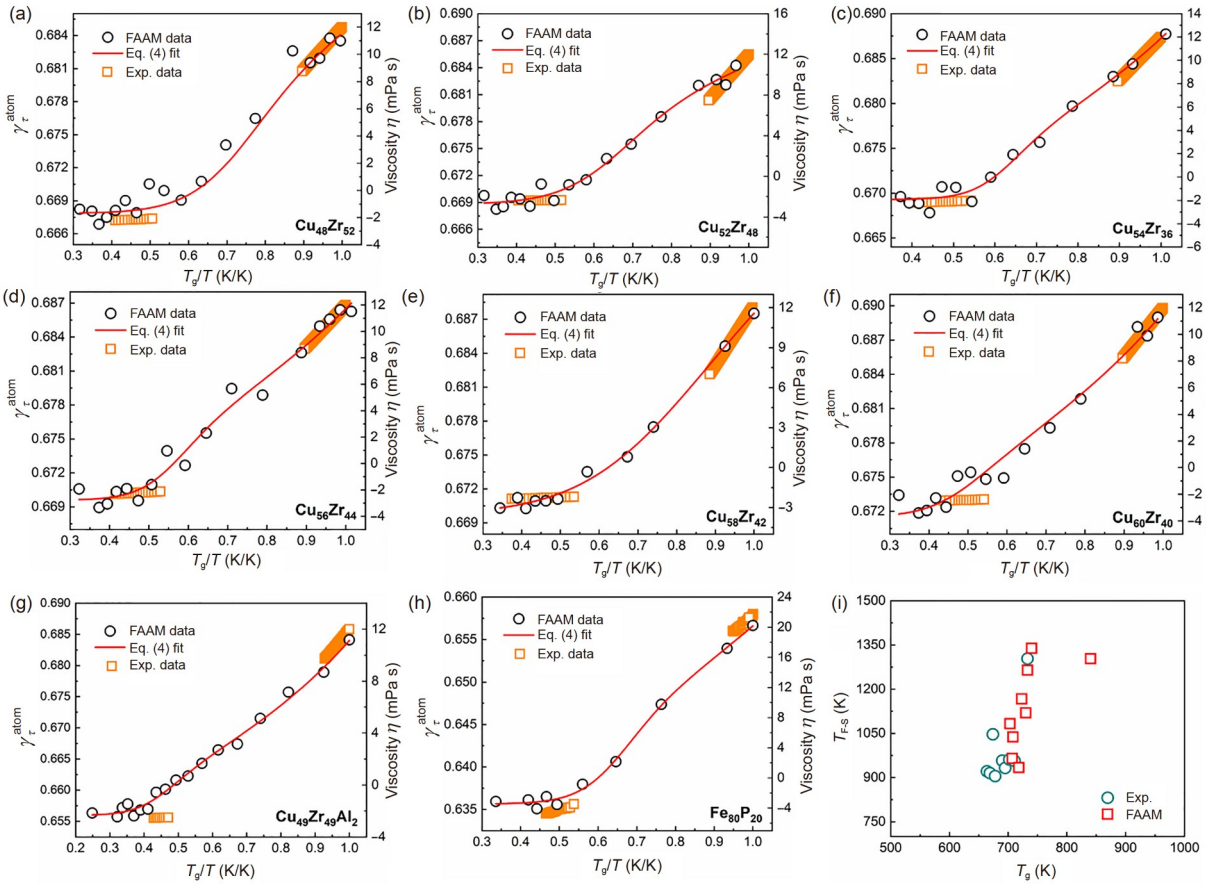

Figure 3 (Color online) The comparison between γ_τ^{atom} and the viscosity η for (a) $Cu_{48}Zr_{52}$ liquid, (b) $Cu_{52}Zr_{48}$ liquid, (c) $Cu_{54}Zr_{46}$ liquid, (d) $Cu_{56}Zr_{44}$ liquid, (e) $Cu_{58}Zr_{42}$ liquid, (f) $Cu_{60}Zr_{40}$ liquid, (g) $Cu_{49}Zr_{49}Al_2$ liquid, and (h) $Fe_{80}P_{20}$ liquid. The hollow black spheres and orange squares represent the data from FAAM and viscosity experiments [11,55,56], respectively. The red curve is the fitted curve using the extended MYEGA model. (i) Comparison of $T_{F\text{-}S}$ obtained from experiments and FAAM calculations, respectively.

Table 1 The parameters of $T_{F\text{-}S}^{atom}$, T_g, f_{FAAM} in simulations, $T_{F\text{-}S}^{\eta}$, f_{exp}, and the crossover temperature of configurational entropy-T_c

Alloys	T_g (K)(MD)	$T_{F\text{-}S}^{\eta}$ (K)	$T_{F\text{-}S}^{atom}/T_g$	$T_{F\text{-}S}^{atom}$ (K)	T_c (K)	f_{exp}	f_{FAAM}
$Cu_{48}Zr_{52}$	707	921.06	1.365	964.9	1193	2.99	3.48
$Cu_{50}Zr_{50}$	730	915.24	1.534	1120	1190	4	4.02
$Cu_{52}Zr_{48}$	703	904.87	1.541	1083	1143	2.53	3.05
$Cu_{54}Zr_{46}$	723	957.52	1.614	1167	1152	3.2	3.32
$Cu_{56}Zr_{44}$	708	932.30	1.466	1038	1061	3.3	4.82
$Cu_{58}Zr_{42}$	718	961.16	1.300	933.8	1163	2.73	2.43
$Cu_{60}Zr_{40}$	733	956.39	1.725	1265	1080	3.1	5.53
$Cu_{49}Zr_{49}Al_2$	740	1047	1.81	1339	1244	3.84	3.17
$Fe_{80}P_{20}$	840	1303.7	1.552	1304	1370	4.75	4.26

3.3 Comparisons between atomic activation and atomic relaxation events

Further, we consider whether atomic relaxation events have a similar capability of mimicking the F-S transition in supercooled liquids. We selected all the local relaxation events in atomic potential energy curves for further analysis. The four variables based on the two-stage division as depicted above were calculated, as shown in Figure S3. Figure 4(a) shows the change of γ_{activ}^{atom} (representing atomic activation events, the same as γ_τ^{atom} in Figure 2(a)) and γ_{relax}^{atom} (equal to $\frac{\tau_{relax}^{atom}}{\tau_{activ}^{atom}}$ in atomic relaxation events) with temperature for $Cu_{50}Zr_{50}$ liquids. The values of them both remain constant at high temperatures and then exhibit monotonic change. Different

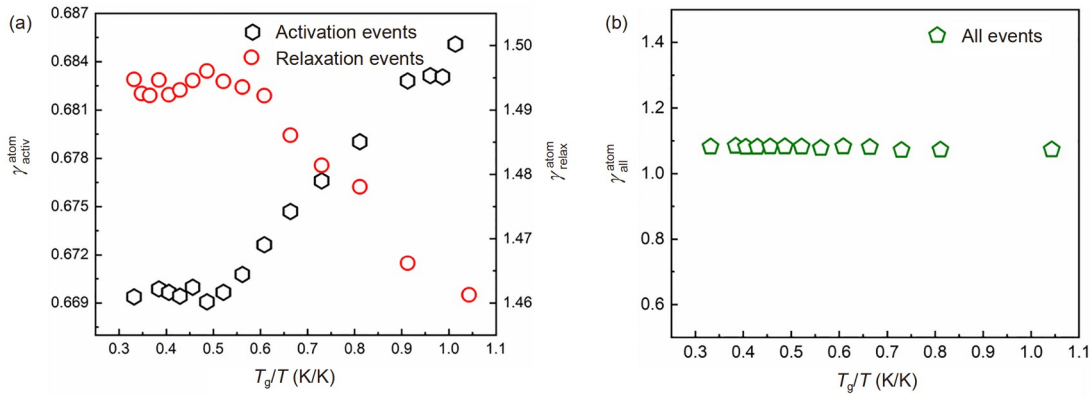

Figure 4 (Color online) Temperature dependence of (a) γ^{atom}_{activ} and γ^{atom}_{relax}, (b) γ^{atom}_{all} during cooling for $Cu_{50}Zr_{50}$ liquid. The black hexagons and red spheres represent the γ^{atom}_{activ} and γ^{atom}_{relax} calculated based on the atomic activation and relaxation events, respectively. The green pentagons denote the γ^{atom}_{all} value calculated based on the above two events.

from the increase of γ^{atom}_{activ} upon cooling, γ^{atom}_{relax} has a negative relationship with temperature. However, if we count two events simultaneously, we could find that the values of γ^{atom}_{all} (the average of γ^{atom}_{activ} plus γ^{atom}_{relax}) do not change at all, as shown in Figure 4(b). During the relaxation of an equilibrium liquid, we can snap these short-time activation and relaxation events from the change in atomic potential energy due to the energy fluctuations. However, as the thermodynamic equilibrium exists, the activation and relaxation events as anti-processes should be essentially complementary. Therefore, only considering the activation events of atoms is already enough to represent all characteristics of the energy fluctuations. This temperature-dependent fluctuation of atomic energy plays an irreplaceable role in F-S transitions.

3.4 The changes of atomic environments

For atomic activation, the local environments around atoms in statistics and then the first neighbors of atoms are crucial to the anomalous energy change [22,57,58]. Here, we capture the local environmental features around the atoms in activation events by quantifying the distance between the activated atom and its neighboring one. The scaled distance distributions at five typical temperatures for $Cu_{50}Zr_{50}$ liquid are shown in Figure 5(a)-(e). To check the interactive behavior of the neighboring atoms, we number neighbor atoms from 1 to 12 by distance and put them on the *x*-axis in order. The *y*-axis is the timesteps used during the activation process. The color represents the distance between the activated atom and the numbered neighbor atoms at a certain timestep. The bluer the color is, the smaller the distance between the activated atom and the neighbor atom, and vice versa. For example, in Figure 5(a), at 1500 K, the color of the No. 8 neighbor atom changes from dark blue to light blue and finally to white with increased timesteps, meaning that this atom first clings to the activated atom and then moves away. The contour map in Figure 5 shows a scattered pattern at HT (Figure 5(a)), and then becomes almost ordered around $T^{atom}_{F\text{-}S}$ ~1100 K (Figure 5(c)) and finally reaches a perfectly ordered state when approaching T_g. This order change can be seen from the distribution of the color shades in the figure. At T_g (Figure 5(e)), two dash red lines can almost divide the map into four-quadrant. Such a change tendency can be illustrated by Figure 5(f), where yellow and other colored (gray and blue) balls denote the activated atom and neighbor atoms, respectively. At 1500 K, the neighbor atoms randomly move. Some atoms (blue ball) move toward the activated atom, while other atoms (grey ball) move away (see the jagged blue and grey areas). When the temperature goes down to $T^{atom}_{F\text{-}S}$ (~1100 K), atoms with similar moving directions appear on the same side of the activated atom. The blue area enclosed by blue atoms gradually becomes smaller as the timestep increases, while the grey area enclosed by grey atoms gradually becomes larger. A stable state can be seen at T_g (730 K). The expansion or reduction of the area represents the transfer of free volume around the activated atom. Figure 5(f) reflects the similar local cooperative motion around the activated atom between $T^{atom}_{F\text{-}S}$ and T_g. Figure 5(g) shows the fractional change in the number of coordination atoms leaving or being replaced before and after the activation event, which could compare the differences in the neighboring atoms between the onset (the situation of ① in Figure 1(a)) and the finish (the situation of ② in Figure 1(a)) of local activation events. By it, we could evaluate the change in atomic diffusion behavior with temperature. Upon cooling, the distribution moves towards a smaller *N* value, indicating that the free diffusion of atoms is gradually limited. At 1500 K, neighboring atoms drastically displace and foreign atoms could come into the first shell, resulting in a disordered motion (Figure 5(a) and (f)). Upon further cooling, the diffusion of atoms begins to be restricted by its surrounding environment, and the prominent performance is

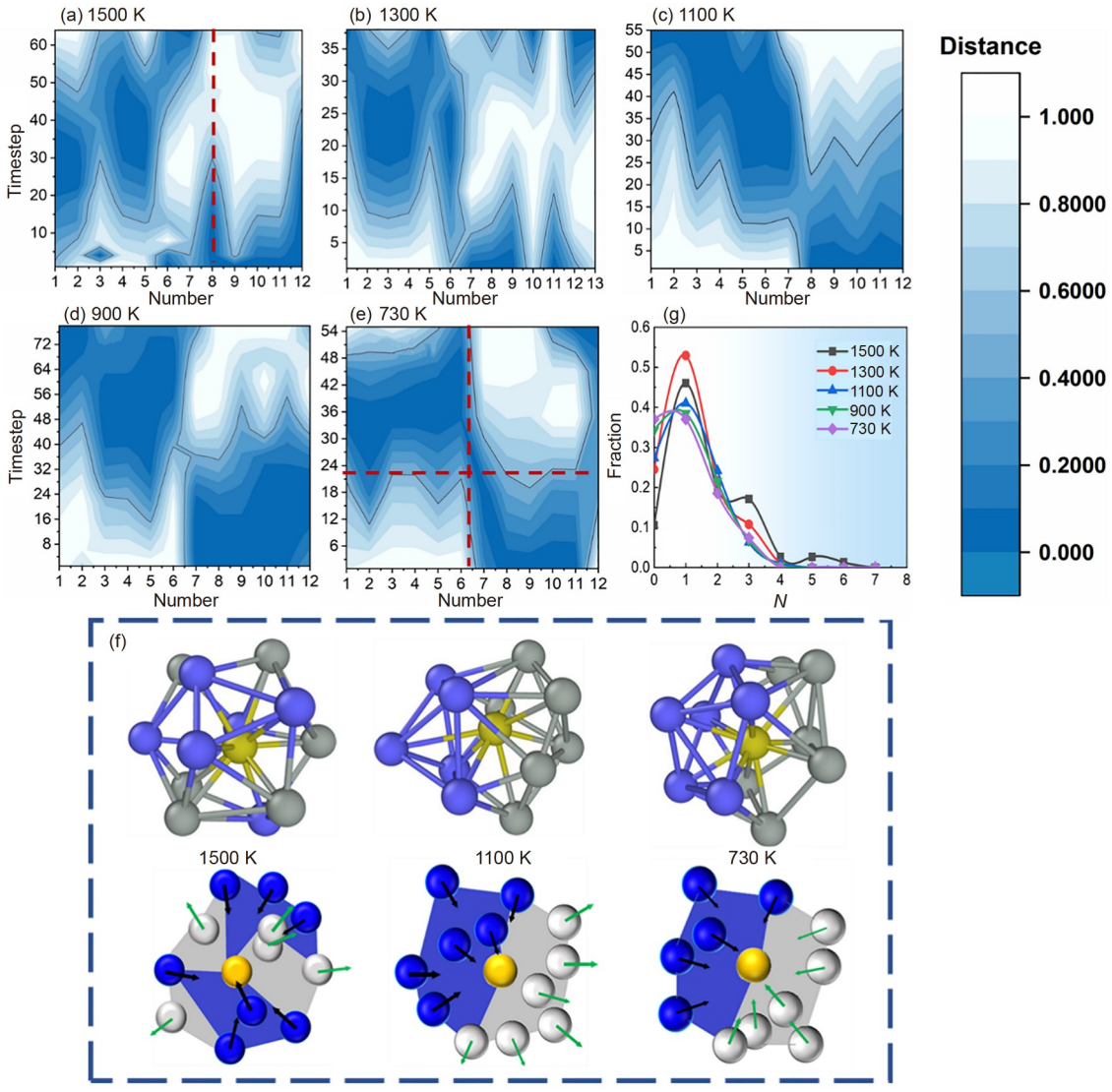

Figure 5 (Color online) Contour map showing the change of distance between the activated atom and its neighboring atoms at (a) 1500 K, (b) 1300 K, (c) 1100 K, (d) 900 K, (e) 730 K in the $Cu_{50}Zr_{50}$ system. (f) The spatial distribution of atoms in the first coordination of the activated atom and their projection on the two-dimensional plane. The yellow ball represents an activated atom, while the gray and blue balls represent the neighboring atoms that are moving away from and approaching the activated atom, respectively. (g) The fractional change in the number of coordination atoms leaving or being replaced before and after the activation event.

the increase of small N (N=0). Especially, when the F-S transition occurred at $T_{\text{F-S}}^{\text{atom}}$ (1100 K), the fraction of atoms with a large N value ($N\geqslant 3$) exhibits a large drop to a small value and then keeps unchanged, meaning that the long-range movements of atoms nearly disappear. This result indicates that the F-S transition is structurally determined by the change of the diffusion mode of atoms upon cooling, due to the local cooperative motion of the neighborhood atoms.

4 Discussion

The F-S transition strength depicted by f has been found to negatively relate to the plasticity of bulk metallic glasses (BMGs) [59]. Such correlation also has been suggested by studies on the F-S transition, relaxation, and Poisson ratio [18,60]. The present work shows that the F-S transition in MGFLs can be reproduced by characterizing the behaviors of atomic activation events. It enables us to make a quantitative prediction of the F-S transition strength f by the parameter $\gamma_{\tau}^{\text{atom}}$. As a result, the parameter $\gamma_{\tau}^{\text{atom}}$ derived from FAAM for various alloys will be a feasible method for investigating the dependence of mechanical properties of BMGs on the dynamic behavior of liquids. Furthermore, a clear local atomic evolution linked to the F-S transition has been given in Figure 5. The F-S transition is a result of the change in atomic diffusion mode associated with the disorder-order free volume transition in the liquid state. Al-

though the parameter $\gamma_\tau^{\text{atom}}$ provides the origin of the F-S transition from the perspective of atomic motions, the driving force behind them remains unclear.

As the temperature drops, the atoms take more and more time to complete the activation process (Figure 1). The reason for this process may be the decrease in the number of activated atoms during the cooling process. According to the energy landscape theory (ELT) [3,61], there are numerous accessible energy poles (energy barriers) and basins (inherent states) for a given material system. By using a similar concept, atoms can be seen as hopping between different basins in Figure 1(c) and (d). The curve of atomic potential energy also can be viewed as the potential energy landscape of every atom, i.e., the atomic potential energy landscape (PEL). This atomic PEL, which is expressed in terms of the evolution of the atomic potential energy with time, is in nature different from the real PEL of the system. For the latter, the system moves around in the basins dependent on the external stimulus. However, the atomic potential energy always fluctuates with time, and the fluctuation feature is dependent on temperature only. Similar to the definition of the system entropy S_c [62-65], We define the entropy $S_{act,c}$ to characterize the chaos of atomic activation events at different temperatures. This entropy is here defined as $S_{act,c}=-\text{sum}(\mu_i \log \mu_i)$ [66], where μ_i is the proportion of the ith types of the atoms with different local environments in activation events. Taking the atoms in a *bcc* crystal as an example, the atoms at different positions have the same local environment, so this entropy is zero. The more diverse the local environment of the atoms, the smaller the value of μ_i, and the larger the value of $S_{act,c}$. The Voronoi tessellation method is an appropriate way to characterize the atomic local environment, so here μ_i is defined as the proportion of the ith kind Voronoi type of the activated atoms. As shown in Figure 6, two turning points of temperature-dependent configuration entropy for $Cu_{50}Zr_{50}$ liquid are present: one is at 1090 K, and another is at 730 K (T_g). The change of enthalpy (H) is also shown in the same figure for comparisons, with no obvious turning. The first turning point for the $S_{act,c}$ is very close to the F-S transition temperature $T_{F\text{-}S}^{\text{atom}}$ (~1120 K), implying that the F-S transition is an entropy-driven process. During the F-S transition, $S_{act,c}$ diminishes more rapidly with a constant slope until the glass transition occurs. This suggests that the atoms in liquids change from a chaotic state to a more uniform state to prepare for the subsequent glass transition. This may explain the experimental observation that a strong glass-forming ability relates to a distinct F-S transition in MGFLs [67]. In addition, the configuration entropy $S_{act,c}$ changes very slowly when the temperature drops below T_g. It is possible for the configuration entropy $S_{act,c}$ to approach a finite, constant value as temperature T approaches a lower temperature or zero. This suggests that a degenerate amorphous ground state may also exist at the atomic scale [68,69]. The configuration entropy can be linked to dynamics through the Adam-Gibbs relation, which suggests that there is a theoretical basis for explaining the F-S transition through thermodynamics, and deserves further study. The $S_{act,c}$ change of other eight liquids with temperature was calculated (see Figure S4) and then the crossover temperature T_c at the first turning points are all obtained (listed in Table 1). Figure 7 shows the relationship between them with their $T_{F\text{-}S}^{\text{atom}}$. The data points for all liquids essentially fall on the line (y=x), implying that $T_{F\text{-}S}^{\text{atom}}$ and T_c are closely connected. Based on the above results, the intrinsic features of the F-S transition have been established as shown in Figure 6. At HT, the basin distribution is dense and the barrier height is larger at high temperatures (according to Figure 1(b)), and hence, the atoms involved in activation events have higher potential

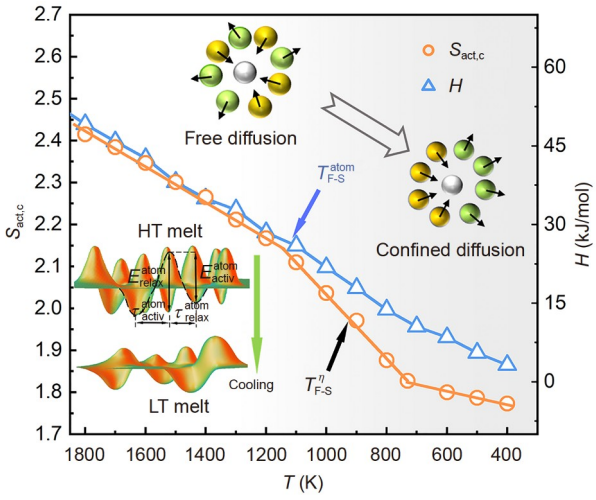

Figure 6 (Color online) Connection map showing the entropy-driven F-S transition. The hollow orange circles and blue triangles represent the entropy $S_{act,c}$, and the enthalpy H, respectively. The insert in the lower left corner is the schematic illustration of the atomic potential energy landscape at HT and LT. The insert in the top right is the schematic illustration of the free volume transition.

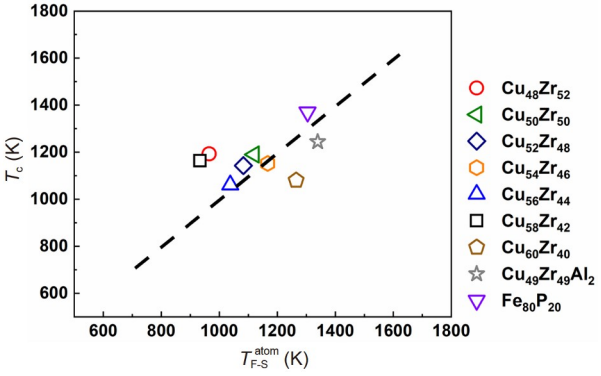

Figure 7 (Color online) The relationship between the F-S transition temperature $T_{F\text{-}S}^{\text{atom}}$ and the transition temperature T_c of the configuration entropy for all systems.

energy with larger energy fluctuation and larger entropy compared to LT. The unstable local environments around atoms lead to the chaos of atom movements in the form of free diffusion. During cooling, the basins distribute sparsely and the activation barrier becomes lower, and the number of atoms participating in activation decreases (Figure S5). At $T_{\mathrm{F\text{-}S}}^{\mathrm{atom}}$, the free diffusion of atoms changes to a confined diffusion mode, and the changes in the free volume around activated atoms begin to become ordered. It is the atomic activation process exhibiting the sudden drop of the chaos of atoms that contributes to the F-S transition.

5 Conclusion

In summary, the F-S transition was discovered by extracting the finite atomic activation events on the atomic potential energy curves. It was found that the dynamic properties of liquid at both HT and LT can be mimicked in this way, and then the characteristics of the F-S transition in liquids are quantitatively predicted by the parameter $\gamma_{\tau}^{\mathrm{atom}}$. Furthermore, the F-S transition is essentially caused by the self-adjusting behavior in their positions within the cage upon cooling, accompanied by a transition from disordered to ordered atomic diffusion. By evaluating the degree of atomic activation chaos in the system, we identified the entropy-driven feature of the F-S transition in supercooled liquids, which was confirmed by the link between the F-S transition temperature and the crossover temperature of configuration entropy. The FAAM, as a representation of temperature-dependent energy fluctuations, provides a new perspective to understanding the liquid dynamics and the glass transition.

This work was supported by the National Natural Science Foundation of China (Grant Nos. 51901139, U1902221, 51971120, and 51971093), the Taishan Scholars Program of Shandong Province (Grant No. tsqn201909010), and the Key Basic and Applied Research Program of Guangdong Province (Grant No. 2019B030302010).

Supporting Information

The supporting information is available online at http://phys.scichina.com and https://link.springer.com. The supporting materials are published as submitted, without typesetting or editing. The responsibility for scientific accuracy and content remains entirely with the authors.

1 M. Mézard, G. Parisi, N. Sourlas, G. Toulouse, and M. Virasoro, Phys. Rev. Lett. **52**, 1156 (1984).
2 Q. Zhai, I. Paga, M. Baity-Jesi, E. Calore, A. Cruz, L. Fernandez, J. Gil-Narvion, I. Gonzalez-Adalid Pemartin, A. Gordillo-Guerrero, D. Iñiguez, A. Maiorano, E. Marinari, V. Martin-Mayor, J. Moreno-Gordo, A. Muñoz-Sudupe, D. Navarro, R. Orbach, G. Parisi, S. Perez-Gaviro, F. Ricci-Tersenghi, J. Ruiz-Lorenzo, S. Schifano, D. Schlagel, B. Seoane, A. Tarancon, R. Tripiccione, and D. Yllanes, Phys. Rev. Lett. **125**, 237202 (2020), arXiv: 2007.03871.
3 P. G. Debenedetti, and F. H. Stillinger, Nature **410**, 259 (2001).
4 Y. C. Hu, F. X. Li, M. Z. Li, H. Y. Bai, and W. H. Wang, J. Appl. Phys. **119**, 205108 (2016).
5 W. Xu, M. T. Sandor, Y. Yu, H. B. Ke, H. P. Zhang, M. Z. Li, W. H. Wang, L. Liu, and Y. Wu, Nat. Commun. **6**, 7696 (2015).
6 N. Ren, L. Hu, L. Wang, and P. Guan, Scripta Mater. **181**, 43 (2020).
7 W. Chu, J. Shang, K. Yin, N. Ren, L. Hu, Y. Zhao, and B. Dong, Acta Mater. **196**, 690 (2020).
8 R. Shi, J. Russo, and H. Tanaka, Proc. Natl. Acad. Sci. U.S.A. **115**, 9444 (2018).
9 I. Saika-Voivod, F. Sciortino, and P. H. Poole, Phys. Rev. E **69**, 041503 (2004), arXiv: cond-mat/0309481.
10 L. Liu, S. H. Chen, A. Faraone, C. W. Yen, and C. Y. Mou, Phys. Rev. Lett. **95**, 117802 (2005), arXiv: cond-mat/0508383.
11 C. Zhou, L. Hu, Q. Sun, H. Zheng, C. Zhang, and Y. Yue, J. Chem. Phys. **142**, 064508 (2015).
12 C. A. Angell, J. Non-Cryst. Solids **73**, 1 (1985).
13 K. Ito, C. T. Moynihan, and C. A. Angell, Nature **398**, 492 (1999).
14 B. W. H. van Beest, G. J. Kramer, and R. A. van Santen, Phys. Rev. Lett. **64**, 1955 (1990).
15 M. Hemmati, C. T. Moynihan, and C. A. Angell, J. Chem. Phys. **115**, 6663 (2001).
16 C. Zhang, L. Hu, Y. Yue, and J. C. Mauro, J. Chem. Phys. **133**, 014508 (2010).
17 S. Wei, P. Lucas, and C. A. Angell, J. Appl. Phys. **118**, 034903 (2015).
18 Q. Sun, C. Zhou, Y. Yue, and L. Hu, J. Phys. Chem. Lett. **5**, 1170 (2014).
19 G. A. Appignanesi, J. A. Rodriguez Fris, and F. Sciortino, Eur. Phys. J. E **29**, 305 (2009).
20 S. Wei, F. Yang, J. Bednarcik, I. Kaban, O. Shuleshova, A. Meyer, and R. Busch, Nat. Commun. **4**, 2083 (2013).
21 Z. Wang, F. Yang, A. Bernasconi, K. Samwer, and A. Meyer, Phys. Rev. B **98**, 024204 (2018).
22 Q. Yang, S. X. Peng, Z. Wang, and H. B. Yu, Natl. Sci. Rev. **7**, 1896 (2020).
23 X. J. Han, and H. R. Schober, Phys. Rev. B **83**, 224201 (2011).
24 G. S. Fanourgakis, J. S. Medina, and R. Prosmiti, J. Phys. Chem. A **116**, 2564 (2012).
25 S. Plimpton, J. Comput. Phys. **117**, 1 (1995).
26 Y. Q. Cheng, H. W. Sheng, and E. Ma, Phys. Rev. B **78**, 014207 (2008).
27 Y. Q. Cheng, E. Ma, and H. W. Sheng, Phys. Rev. Lett. **102**, 245501 (2009).
28 G. J. Ackland, M. I. Mendelev, D. J. Srolovitz, S. Han, and A. V. Barashev, J. Phys.-Condens. Matter **16**, S2629 (2004), arXiv: cond-mat/0406356.
29 W. G. Hoover, Phys. Rev. A **31**, 1695 (1985).
30 G. Voronoi, J. Reine Angew. Math. (Crelles J.) **134**, 198 (1908).
31 U. Ramamurty, M. L. Lee, J. Basu, and Y. Li, Scr. Mater. **47**, 107 (2002).
32 W. H. Wang, Prog. Mater. Sci. **106**, 100561 (2019).
33 S. V. Ketov, Y. H. Sun, S. Nachum, Z. Lu, A. Checchi, A. R. Beraldin, H. Y. Bai, W. H. Wang, D. V. Louzguine-Luzgin, M. A. Carpenter, and A. L. Greer, Nature **524**, 200 (2015).
34 L. Zhang, Y. Wang, Y. Yang, and J. Qiao, Sci. China-Phys. Mech. Astron. **65**, 106111 (2022).
35 G. Ding, F. Jiang, X. Song, L. Dai, and M. Jiang, Sci. China-Phys. Mech. Astron. **65**, 264613 (2022).
36 R. J. Xue, L. Z. Zhao, C. L. Shi, T. Ma, X. K. Xi, M. Gao, P. W. Zhu, P. Wen, X. H. Yu, C. Q. Jin, M. X. Pan, W. H. Wang, and H. Y. Bai, Appl. Phys. Lett. **109**, 221904 (2016).
37 M. De Marzio, G. Camisasca, M. Rovere, and P. Gallo, J. Chem. Phys. **146**, 084502 (2017).
38 P. W. Anderson, B. I. Halperin, and C. M. Varma, Philos. Mag. **25**, 1 (1972).
39 G. T. Barkema, and N. Mousseau, Phys. Rev. Lett. **77**, 4358 (1996), arXiv: cond-mat/9607156.
40 Y. Fan, T. Iwashita, and T. Egami, Nat. Commun. **5**, 5083 (2014).

41 S. A. Trygubenko, and D. J. Wales, J. Chem. Phys. **120**, 2082 (2004), arXiv: cond-mat/0402209.
42 F. Boioli, T. Albaret, and D. Rodney, Phys. Rev. E **95**, 033005 (2017).
43 S. Swayamjyoti, J. F. Löffler, and P. M. Derlet, Phys. Rev. B **93**, 144202 (2016).
44 J. C. Mauro, Y. Yue, A. J. Ellison, P. K. Gupta, and D. C. Allan, Proc. Natl. Acad. Sci. **106**, 19780 (2009).
45 Q. Zheng, J. C. Mauro, A. J. Ellison, M. Potuzak, and Y. Yue, Phys. Rev. B **83**, 212202 (2011).
46 C. Z. Zhang, L. N. Hu, X. F. Bian, and Y. Z. Yue, Chin. Phys. Lett. **27**, 116401 (2010).
47 N. A. Mauro, M. Blodgett, M. L. Johnson, A. J. Vogt, and K. F. Kelton, Nat. Commun. **5**, 4616 (2014).
48 R. Novakovic, M. L. Muolo, and A. Passerone, Surf. Sci. **549**, 281 (2004).
49 M. Mohr, R. K. Wunderlich, S. Koch, P. K. Galenko, A. K. Gangopadhyay, K. F. Kelton, J. Z. Jiang, and H. J. Fecht, Microgravity Sci. Technol. **31**, 177 (2019).
50 H. Zhang, C. Zhong, J. F. Douglas, X. Wang, Q. Cao, D. Zhang, and J. Z. Jiang, J. Chem. Phys. **142**, 164506 (2015).
51 A. Jaiswal, T. Egami, K. F. Kelton, K. S. Schweizer, and Y. Zhang, Phys. Rev. Lett. **117**, 205701 (2016), arXiv: 1604.08920.
52 T. Iwashita, D. M. Nicholson, and T. Egami, Phys. Rev. Lett. **110**, 205504 (2013), arXiv: 1304.6784.
53 H. B. Yu, Z. Wang, W. H. Wang, and H. Y. Bai, J. Non-Cryst. Solids **358**, 869 (2012).
54 B. Li, K. Lou, W. Kob, and S. Granick, Nature **587**, 225 (2020), arXiv: 2008.09385.
55 R. Parthiban, M. Stoica, I. Kaban, I. Ravi Kumar, and J. Eckert, Intermetallics **66**, 48 (2015).
56 X. Zhai, X. Li, Z. Wang, L. Hu, K. Song, Z. Tian, and Y. Yue, Acta Mater. **239**, 118246 (2022).
57 H. Zhang, X. Wang, H. B. Yu, and J. F. Douglas, J. Chem. Phys. **154**, 084505 (2021), arXiv: 2101.12104.
58 Z. Wang, and W. H. Wang, Natl. Sci. Rev. **6**, 304 (2019).
59 T. Wang, L. Hu, Y. Liu, and X. Hui, Mater. Sci. Eng.-A **744**, 316 (2019).
60 Q. Sun, L. Hu, C. Zhou, H. Zheng, and Y. Yue, J. Chem. Phys. **143**, 164504 (2015).
61 M. D. Ediger, M. Gruebele, V. Lubchenko, and P. G. Wolynes, J. Phys. Chem. B **125**, 9052 (2021).
62 S. Sastry, Nature **409**, 164 (2001), arXiv: cond-mat/0011317.
63 T. Odagaki, and A. Yoshimori, J. Non-Cryst. Solids **355**, 681 (2009).
64 M. Goldstein, J. Chem. Phys. **64**, 4767 (1976).
65 G. P. Johari, J. Chem. Phys. **112**, 7518 (2000).
66 B. Yu, Y. Liang, Z. Tian, Y. Zhang, Q. Xie, T. Gao, and Y. Mo, J. Non-Crystalline Solids **522**, 119578 (2019).
67 L. Xue, L. Shao, Q. Luo, L. Hu, Y. Zhao, K. Yin, M. Zhu, L. Sun, B. Shen, and X. Bian, J. Mater. Sci. Tech. **77**, 28 (2021).
68 F. Smallenburg, and F. Sciortino, Nat. Phys. **9**, 554 (2013).
69 E. Zaccarelli, I. Saika-Voivod, S. V. Buldyrev, A. J. Moreno, P. Tartaglia, and F. Sciortino, J. Chem. Phys. **124**, 124908 (2006), arXiv: cond-mat/0511433.